Performance Optimization of Antenna-Coupled Al/AlO$_x$/Pt Tunnel Diode Infrared Detectors

Jeffrey A. Bean, *Member, IEEE*, Arthur Weeks, *Senior Member, IEEE*, and
Glenn D. Boreman, *Senior Member, IEEE*

Abstract—Signal-to-noise ratio (SNR) is a valuable figure of merit in determining the operating scope of infrared detectors. Antenna-couple metal–oxide–metal diodes have been shown to detect infrared radiation without cooling or applied bias, but so far have been hampered by their SNR. This paper details a comprehensive study of the fabrication parameters that control the formation of the tunneling oxide barrier to optimize the performance of these detectors. Since the tunneling barrier affects both current-voltage and infrared detection characteristics, fabrication parameters can be optimized to improve device performance. The current–voltage characteristics of the devices are detailed in this paper; resistance, nonlinearity, and curvature coefficient are parameterized on fabrication procedures. Infrared detection characteristics are detailed and SNR is studied as a function of device nonlinearity and biasing conditions.

Index Terms—Antennas, infrared detectors, infrared measurements, thin film devices, tunnel diodes.

I. Introduction

ANTENNA-coupled metal–oxide–metal (MOM) diode infrared detectors have been the subject of increasing interest due to their small size, CMOS compatibility, and ability to offer full functionality without cooling or applied bias [1]–[6]. Although thin-film MOM devices were introduced in the 1970s [7]–[9], efforts to increase device performance since then have not focused on fabrication parameters, but rather on understanding the operating characteristics of the antenna and diode. Studies have been performed to increase responsivity with substrate-side illumination [10], implement broadband antennae [11], increase operating frequencies to the visible [12], and demonstrate dual-band infrared/millimeter wave detection [13]. However, no study has yet been performed to optimize device response based on the fabrication parameters of the MOM diode.

This paper focuses on a single device geometry and substrate stack so that the operating characteristics of the MOM diode can be studied. Most studies on thin-film MOM diodes have been of the symmetric variety, where the same metal is used for each side of the oxide barrier [1], [3], [14]–[16].

J. A. Bean and G. D. Boreman are with the College of Optics and Photonics, University of Central Florida, Orlando, FL 32816 USA (e-mail: jbean@mail.ucf.edu).

A. Weeks is with the Department of Electrical Engineering and Computer Science, University of Central Florida, Orlando, FL 32816 USA (e-mail: weeks@mail.ucf.edu).

Although asymmetric point-contact diodes were introduced in the 1960s [17]–[20], the thin-film variety were not implemented until 2006 [21]. For an asymmetric diode structure, nonlinearity appears in the current-voltage (*I–V*) characteristic that is asymmetric with respect to zero bias. This is of note because the *I–V* characteristic of a MOM diode gives rise to the performance that can be expected, including zero-bias detection, for asymmetric diode devices. The *I–V* characteristic applies from d.c. up to optical frequencies due to the femtosecond tunneling time of an electron through a thin barrier in an MOM diode [8].

The *I–V* characteristic is dependent upon the comprising materials of the diode and thickness of the oxide barrier. For this, the diode type chosen is Al/AlO$_x$/Pt, where aluminum oxide (AlO$_x$) is grown on the Al to create a barrier. The fabrication parameters are varied such that the thickness of the AlO$_x$ can be controlled, resulting in the ability to control device resistance and curvature. The fabrication procedure used to manufacture these devices will be presented in detail along with the *I–V* characteristics as a function of those fabrication parameters.

An equivalent circuit model for the device is presented to provide a basis for the antenna-coupled MOM diode design. Energy band diagrams are shown to describe the mechanism that allows the detection of infrared radiation in these devices, known as Fermi level modulation.

A comprehensive noise study, including the amplification circuitry, is presented so that the signal-to-noise ratio (SNR) can be accurately determined for a given infrared irradiance. The device nonlinearity, which is the second derivative of the *I–V* characteristic, is studied for various fabrication parameters. Ultimately, the affect of nonlinearity and bias on device SNR is analyzed.

II. Device Operation and Design

A. MOM Diode Rectification

There are many possible mechanisms that can describe the flow of electrons in an antenna-coupled MOM diode [9], [10], such as photon-assisted tunneling [9], [24], [25], photon-assisted surmounting of the barrier [26], [27], thermally assisted tunneling [9], [15], [20], and field-assisted tunneling (also known as Fermi level modulation) [9]. In every case, current flows from one metal electrode to the other. It should be noted that this electrical conduction can arise from various mechanisms that can be either classical or quantum mechanical. In addition, trap states in the tunnel barrier can
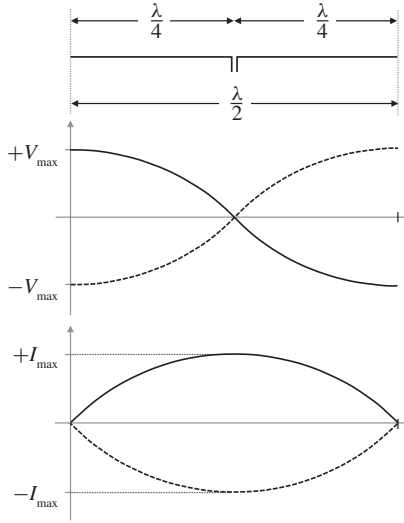
Fig. 1. Dipole antenna with corresponding voltage and current distributions for two waves separated in phase by 180°. A maximum in current occurs at the feed point, or diode, while the voltage maxima occur at the ends of the dipole.

Fig. 2. MOM diode band diagrams at (a) equilibrium and (b) under infrared illumination.

impact the conduction mechanisms as well, since electrons can occupy vacant trap states and tunnel from one metal to the other in multiple steps [28].

Any number of the aforementioned conduction mechanisms can occur simultaneously in an MOM diode [26], [27]. However, based on the wavelength of the irradiation and the measurement of specific response characteristics, it is possible to distinguish the mechanism giving rise to the device response. Photon-assisted tunneling is expected to dominate for photon energies that are approximately equal to the barrier height [27], which in the case of Al/AlO$_x$/Pt devices for this paper is approximately 2 eV [29]. For radiation in the long-wave infrared (LWIR), tunneling due to Fermi-level modulation is shown to dominate.

The basis for field-assisted tunneling can best be described by examining the voltage and current distributions along a dipole antenna. For a half-wavelength dipole, approximations of the voltage and current distributions are shown in Fig. 1, where the feed point (MOM diode in this case) is located at the center.

Field-assisted tunneling involves the perturbation of a barrier between two metals. When infrared radiation is incident upon the antenna-coupled MOM diode structure, an optical or infrared alternating current (a.c.) voltage is induced at the diode [9], [10], creating a field within the oxide tunneling barrier. The induced time-dependent bias sums with any d.c. applied bias on the device. This time-dependent bias $V(t)$ can be expressed as

$$V(t) = V_b + V_{IR}\cos(\omega t) \tag{1}$$

where V_b is the applied d.c. bias, V_{IR} is the amplitude of the induced voltage, and ω is the angular frequency of the incident radiation [9], [30].

An energy band diagram of a MOM diode at equilibrium is shown in Fig. 2(a). Although the barrier shape changes due to image forces caused by populated electron states in the metal
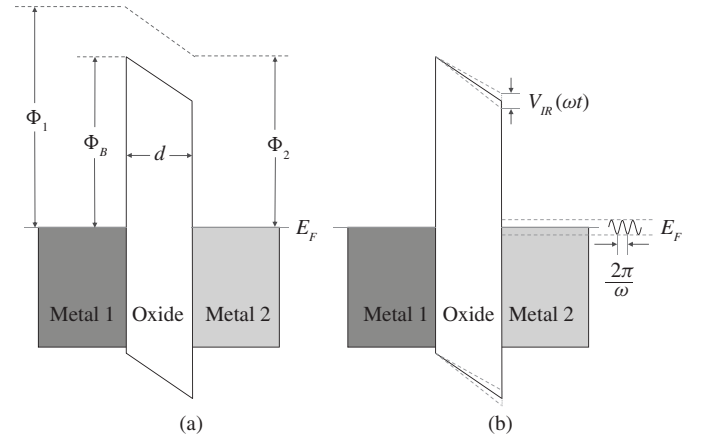
for a finite temperature [31], a trapezoidal barrier is sufficient for explanation of the rectification phenomenon. The structure in Fig. 2(a) features dissimilar metals of work functions ϕ_1 and ϕ_2, interface barrier height ϕ_B, and an oxide barrier of thickness d. In an unbiased structure, the Fermi levels of the metals align to reach equilibrium and the energy bands bend within the oxide layer, resulting in a built-in field. This built-in field is equal to the difference in the work functions of the metals divided by the thickness of the barrier. For an Al/AlO$_x$/Pt diode, the built-in field across a 2-nm AlO$_x$ layer is approximately 6.85 MV/cm.

When the induced voltage causes a forward bias such that the Fermi level of metal 2 is reduced to an energy level below that in metal 1, the field strength in the barrier increases and the potential barrier thickness decreases [2]. Therefore, the probability for an electron to tunnel through the potential barrier from left to right increases, as does the overall tunneling current in the structure. Conversely, when the induced voltage causes a reverse bias such that the Fermi level of metal 2 is increased to an energy level above that in metal 1, the field strength in the barrier decreases and the potential barrier thickness increases. Thus, the tunneling probability of an electron through the potential barrier decreases. This nonlinear tunneling behavior, which is derived from the asymmetry in the diode, leads to a net current flow in one direction and allows the MOM diode to act as a rectifier.

Since tunneling is an inherently fast process [8], MOM diodes have shown to be capable of rectifying high-frequency signals in the LWIR [32]–[34], mid-IR [23], [35], and even up to optical frequencies [12], [22], [36].

B. Modeling and Equivalent Circuit Model

The rectification process was described using energy band diagrams and electron tunneling through a barrier, but the overlap area of the MOM diode must be small enough so that the RC time constant is less than one infrared wave cycle [15]. An equivalent circuit of an antenna-coupled MOM diode under incident infrared radiation can be modeled as an antenna and diode connected in series [24], [30], as shown in Fig. 3.

The MOM diode can be described by a junction capacitance C_D in parallel with a nonlinear voltage-dependent
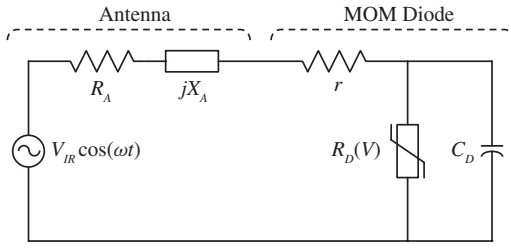
Fig. 3.   Equivalent-circuit model of an antenna-coupled MOM diode. As a receiver, the antenna is represented by a voltage source with series impedance. The diode is represented by the parallel combination of a capacitor and voltage-controlled resistor in series with the lead impedance.
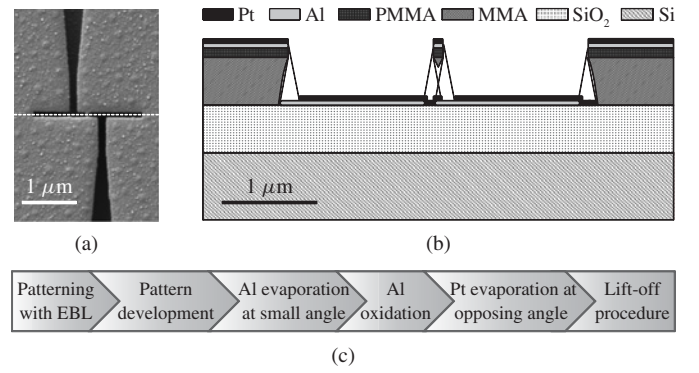

Fig. 4.   (a) Top view and (b) cross-section of the exposed resist after the development and subsequent shadow evaporation. The PMMA bridge allows for the formation of the MOM diode. (c) Summary of the fabrication process flow.

resistance $R_D(V)$. This parallel combination is in series with the resistance r, which represents metal-lead and/or spreading resistance [30]. An antenna functioning as a receiver can be represented by an alternating current source $V_{IR}\cos(\omega t)$, which is the induced time-dependent bias discussed in the previous section. This is connected in series with impedance $R_A + jX_A$, where R_A is the real impedance of the source and jX_A is zero at the resonant frequency. For this circuit, the RC time constant is the product of the diode capacitance and the equivalent resistance, which is R_D in parallel with the series combination of R_A and r. This leads to a cut-off frequency f_c of

$$f_c = \frac{1}{2\pi RC} = \frac{R_A + r + R_D(V)}{2\pi (R_A + r)R_D(V)C_D}. \tag{2}$$

While rectification and mixing are still observed above this frequency, it is with diminished efficiency. To minimize the response time of the diode and attain a high cut-off frequency, the diode capacitance must be small. If the capacitor considered is a small parallel plate capacitor, the diode capacitance C_D is

$$C = \frac{\varepsilon_{ox}\varepsilon_0 A}{d} \tag{3}$$

where ε_{ox} is the relative permittivity of the oxide in the MOM diode, ε_0 is the permittivity of free space, A is the junction area, and d is the thickness of the dielectric. For a diode with a 25-Å barrier composed of Al_2O_3, with a relative permittivity at 28.3 THz approximately equal to 1 [37] and an equivalent resistance of 1 kΩ, a 75×75 nm or smaller overlap area is required to obtain a cut-off frequency high enough to rectify 10.6-μm incident radiation.

III. FABRICATION

A. Device Fabrication

The fabrication of antenna-coupled MOM diodes using shadow evaporation has been previously reported [5], but specific processing parameters form the basis of this paper and, as such, will be detailed. The antenna and electrical lead geometry is patterned via electron beam lithography (EBL) with a bi-layer poly(methyl methacrylate) (PMMA)/MMA resist stack on a Si substrate with a 1.19-μm SiO_2 electrical insulation layer. The underlying MMA is a more sensitive resist which, for a specified thickness and exposing electron beam accelerating voltage, forms an undercut beneath the top PMMA layer. After EBL, the pattern is developed using

MIBK:IPA (1:3), and a descum procedure is performed with O_2 plasma to remove any undesired residual resist.

Fig. 4(a) shows a top view of exposed resist after development and metal deposition. Fig. 4(b) is a cross section of the same structure, along the antenna axis, indicated by the dotted line in the top view. When the patterns for each half of the dipole halves are properly spaced, a bridge of PMMA remains while removing the underlying MMA. This forms the basis behind the shadow evaporation fabrication procedure [38], which allows formation of the MOM diode with a single lithography step.

The first metal deposition is performed with the sample oriented at a small angle with respect to normal, with the rotation about the PMMA bridge. Evaporation was chosen as the deposition method because it offers a directional non-conformal deposition through the patterned resist. Shown by the light gray aluminum layer in Fig. 4(b), the aluminum layer is deposited through the pattern in the developed PMMA shown in Fig. 4(a). Aluminum is chosen because it readily forms a native oxide layer when exposed to oxygen [29], which at atmospheric pressure is approximately 22–25 Å thick, depending upon laboratory conditions such as temperature and humidity [5]. After an oxide layer is grown on the deposited aluminum, platinum is deposited at an opposing angle to the first deposition, shown in Fig. 4(b) by the black layer. The deposition angles are determined by the thickness of the resist and the available undercut of the MMA layer. The diode overlap area can be controlled by the geometry of the PMMA bridge and the deposition angles. After a lift-off procedure, the antenna-coupled MOM diode is completed. A scanning electron micrograph of a completed device is shown in Fig. 5. The inset image shows the overlap area, which for this case is approximately 75×75 nm.

B. Tunneling Barrier Growth Process

The crucial factor in the fabrication procedure is the oxidation of the aluminum, which forms the tunneling barrier in the MOM diode. Diodes fabricated with an oxidation at atmospheric pressure have shown to be of very high resistance [5]. Therefore, it is desirable to oxidize the aluminum with a controllable pressure of oxygen, which allows for a thinner
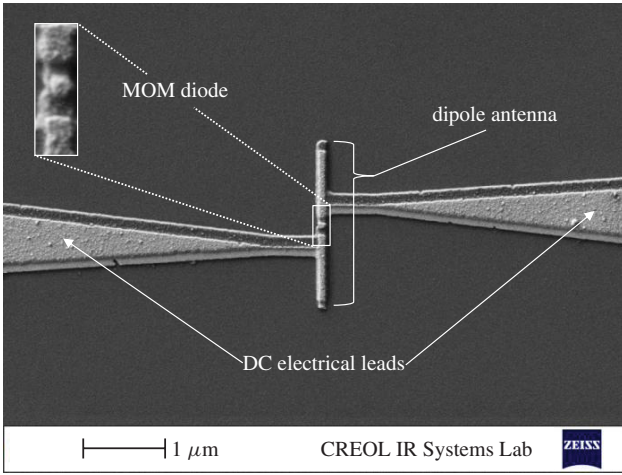
Fig. 5. Scanning electron micrograph of completed antenna-coupled MOM tunnel diode infrared detector after shadow evaporation and liftoff. The inset image shows the overlap of the two metal layers, which are separated by a thin AlO$_x$ layer grown by the intermediate oxidation step.

Fig. 6. *In situ* ellipsometry of AlO$_x$ growth on aluminum thin film. The O$_2$ valve was opened at $t = 0$ min and the flow of oxygen was started at $t = 3$ min. The film reaches a thickness of approximately 6 Å after 15 min.

oxide layer to be formed than with air oxidation, providing lower resistance devices.

The oxidation of a thin film of aluminum at room temperature results in an AlO$_x$ barrier which reaches a diffusion-limited thickness based on the pressure. *In situ* ellipsometry was performed to analyze the oxidation of aluminum film under vacuum. The base partial pressure of O$_2$ of during the evaporation was 5.7×10^{-10} Torr, as measured with a residual gas analyzer. Assuming a unity sticking coefficient for oxygen, a monolayer of AlO$_x$ would take on the order of 65 min to form [39], allowing for the assumption that the aluminum film starts without any AlO$_x$. The ellipsometry from the growth of aluminum oxide at room temperature for a 10-μTorr oxidation is shown in Fig. 6, which is consistent with *in situ* aluminum oxidation performed by Lindmark *et al.* [40].

The AlO$_x$ film never completely stops growing, but after the initial 15 min, the rate decreases to approximately 1 Å per h. As such, the oxidations that form the MOM diode are performed for 30 min, which has shown to be repeatable and reliable. Low pressure *in situ* oxidation is the only way to accurately control the AlO$_x$ oxide thickness grown [5]. It is utilized in this paper so that its effect on diode characteristics can be studied, allowing for the ability to tailor the *I–V* characteristics. Experiments performed studying this paper have also shown that yield is improved for low-pressure oxidation and by the precision of the device fabrication. Changes in the oxidation partial pressure could cause variations in grain size, packing density, and grain boundary defects in the AlO$_x$ barrier. Although these variations could certainly affect the tunneling properties of the AlO$_x$ barrier, the changes caused by oxidation partial pressure were only characterized from an electrical and infrared response standpoint.

MOM diodes that are fabricated using two lithography steps not only require alignment of multiple layers but can only be fabricated at the expense of either oxide thickness or diode overlap area. If a two-lithography process is utilized, the sample is exposed to ambient conditions and the full native oxide thickness is grown on the aluminum. Tiwari *et al.*
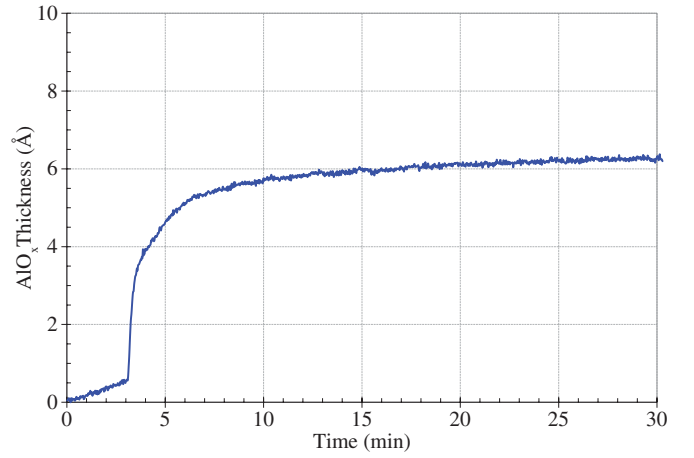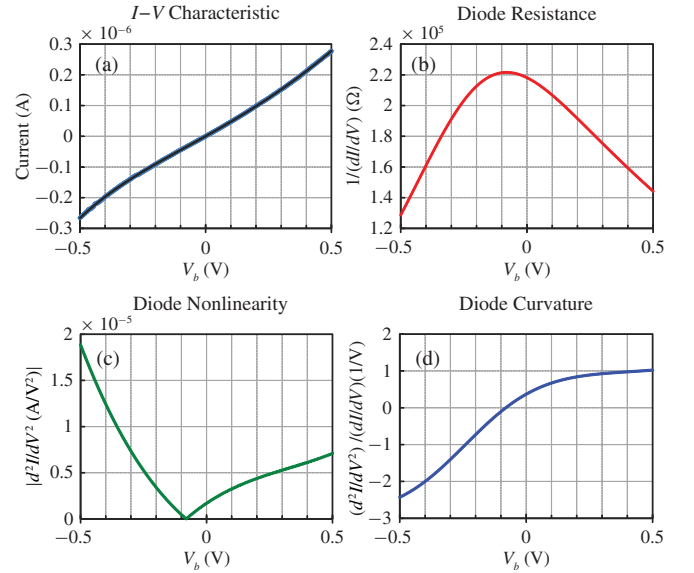

Fig. 7. (a) *I–V* characteristic, (b) resistance, (c) nonlinearity, and (d) curvature of Al/AlO$_x$/Pt antenna-coupled MOM diode. The measured *I–V* characteristic is fitted with a fifth-order polynomial, which is then used to calculate the other parameters used for comparison.

showed that this native oxide layer could be removed by means of an in-vacuum ion etching source and regrown using low-pressure oxidation before the second metal evaporation. However, this etching procedure also etches the patterning resist, so it comes with the expense of losing control of the diode overlap area [6]. Therefore, a single lithography process was used to provide for the most precise geometry from device to device, and from one fabrication run to the next.

IV. MEASUREMENTS

A. I–V Characterization

The *I–V* characteristics of MOM diode-based devices can be measured to study the effect of design and fabrication parameters. The *I–V* characteristic of an antenna-coupled Al/AlO$_x$/Pt MOM diode is shown in Fig. 7(a). The data is acquired by
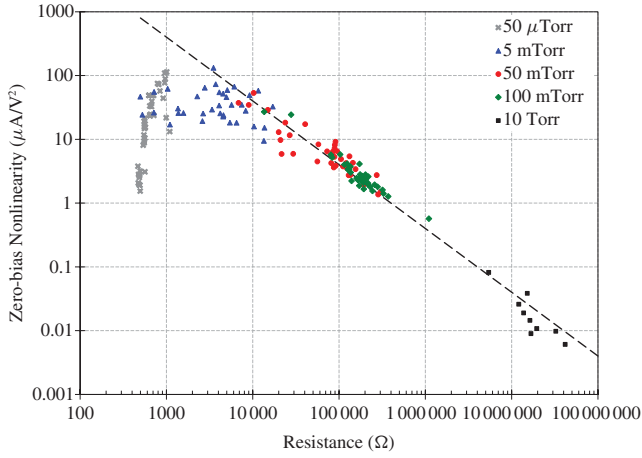
Fig. 8.   Zero-bias nonlinearity as a function of Al/AlO$_x$/Pt zero-bias diode resistance for various oxidation pressures. As oxidation pressure increases, the thickness of the AlO$_x$ increases, which results in higher device resistance. Diode nonlinearity is inversely proportional to the diode resistance.

Fig. 9.   Zero-bias curvature as a function of Al/AlO$_x$/Pt zero-bias diode resistance for various oxidation pressures. As oxidation pressure increases, the oxide thickness increases and the diode curvature increases.

measuring the current as the bias V_b is swept and fitted with a fifth-order polynomial. From the measured I–V characteristic, the resistance is defined as

$$R_V = \left(\left. \frac{dI}{dV} \right|_{V=V_b} \right)^{-1} \qquad (4)$$

and is shown in Fig. 7(b), where R_V is the resistance of the diode evaluated at the bias voltage V_b of interest. Although the asymmetry in the I–V characteristic appears as minimal, Fig. 7(b) shows that device resistance changes by approximately a factor of 2 from zero bias to ±0.5-V.

The second derivative of the current is referred to as the nonlinearity of the device, is expressed as

$$N_V = \left. \frac{d^2 I}{dV^2} \right|_{V=V_b}. \qquad (5)$$

The absolute value of N_v is shown in Fig. 7(c) as a function of V_b. When evaluated at zero bias ($V_b = 0$-V), diode nonlinearity is proportional to the constant coefficient of the second-order term of the Taylor series expansion of the I–V characteristic. The curvature (also referred to as sensitivity) of the diode is the product of the resistance and the nonlinearity [41], defined as

$$S_V = \left. \frac{\frac{d^2 I}{dV^2}}{\frac{dI}{dV}} \right|_{V=V_b} \qquad (6)$$

where S_V is evaluated at the bias voltage of interest. This is shown in Fig. 7(d) for an Al/AlO$_x$/Pt MOM diode.

Resistance, nonlinearity, and curvature are compared at zero-bias since all of the infrared measurements have been performed at zero bias, with exception of the bias-dependent measurement. The rectified voltage from the diode is proportional to the curvature of the diode, and the rectified current is proportional to the second derivative of the current [22]. For these experiments, the rectified current is measured with a low-noise current amplifier. As such, it is desired to fabricate MOM diodes with large nonlinearity from the
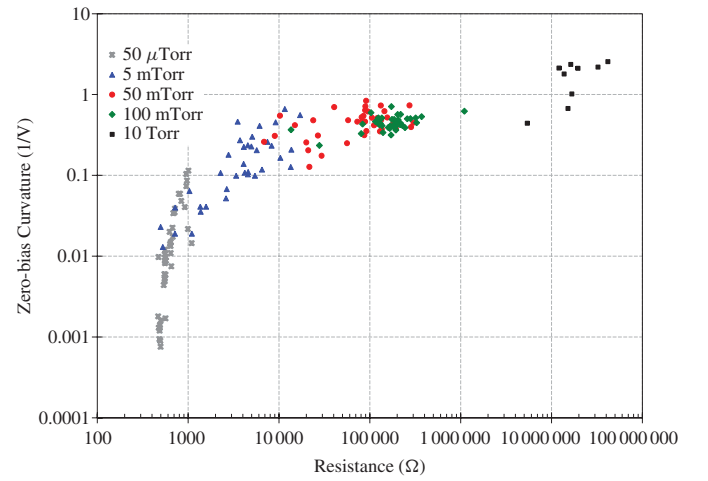
I–V characteristic to provide for a large response. Fig. 8 shows the zero-bias nonlinearity for individual Al/AlO$_x$/Pt MOM diodes as a function of zero-bias resistance for various oxidation pressures, which are shown in the legend. Diode resistance increases as a function of the oxidation pressure. The nonlinearity is inversely proportional to the resistance of the diode, and a linear fit is shown by the dotted line.

At diode resistances of less than 5 kΩ, the nonlinearity ceases to follow the trend. For 50 μTorr and 5 mTorr oxidation, approximately 6 and 10 Å layer of AlO$_x$ is grown, respectively. These thicknesses only constitute a few monolayers of oxide and, as such, it is believed that pinholes and localized thinning of the oxide can impact the functionality of the MOM diodes [42]. The data shows that the devices fabricated with 100 mTorr oxidation exhibit the least scatter and most predictable nature. This is due to the fact that, for the system used in this paper, it is easiest to precisely control pressures at 100 mTorr. For higher oxidation pressures, such as 10 Torr, the devices exhibit behavior similar to those oxidized in atmosphere, meaning that the native oxide thickness of 22–25 Å is reached near 10 Torr at room temperature. These devices have lower yield than those formed with low-pressure oxidation.

Similar behavior can be seen by looking at the zero-bias curvature of individual Al/AlO$_x$/Pt MOM diodes as a function of zero-bias resistance, shown in Fig. 9.

Again, for resistances less than 5 kΩ, diode curvature falls off faster than the trend of the other oxidation pressure cases. As the tunneling barrier gets thinner and thinner, the diode exhibits resistive behavior, which causes the curvature to approach zero. Table I provides a summary of the various diode parameters as a function of oxidation pressure found in this paper.

B. Noise Characterization

To accurately determine the SNR of a device for a given infrared irradiance, the various sources of noise must be analyzed. The device under test (DUT) is placed at the focus

TABLE I
DIODE PARAMETERS VERSUS OXIDATION PRESSURE

Oxidation pressure	Average resistance (Ω)	Nonlinearity (μA/V^2)	Curvature (V^{-1})
50 μTorr	655	29.09	0.022
5 mTorr	5.02 k	39.04	0.180
50 mTorr	97.9 k	9.336	0.457
100 mTorr	201.8 k	3.862	0.452
10 Torr	20.39 M	0.024	1.696

As the oxidation pressure is increased, the average zero-bias resistance of the diodes increases, as does the curvature. Zero-bias nonlinearity is inversely proportional to the zero-bias resistance of the diode. For oxidation pressures of 5 mTorr or less, it has been found that for the Al/AlO$_x$/Pt material set, the barrier thickness is thin enough that diode characteristics are heavily impacted by localized tunneling in thinner parts of the barrier.
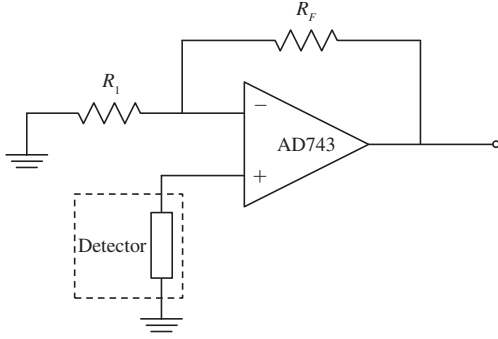
Fig. 10. Operational amplifier circuit used for infrared device measurements. The input to the amplifier is derived from infrared frequency currents that are rectified by the diode. The detector enclosed by the dotted line denotes the equivalent circuit model of the antenna-coupled MOM diode shown in Fig. 3.
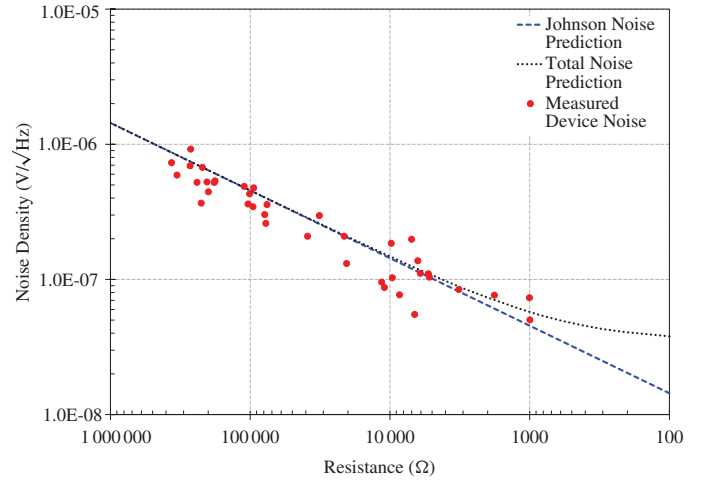
Fig. 11. Johnson noise and total noise predictions as well as measured device noise as a function of diode resistance. The data shows that Johnson noise is the dominant source of noise.

of a CO_2 laser beam. The DUT is connected to an Analog Devices AD743 operational amplifier. The circuit diagram for a connected device is shown in Fig. 10.

By superposition of powers, there are seven internal noise sources present in the circuit used to measure the devices, shown in (7). Each component in the noise calculation is computed based on the elements in operational amplifier circuit and includes the voltage and current noise inherent to the AD743 amplifier. From the data sheet, the input voltage noise density e_n of the AD743 amplifier is 3.2 nV/$\sqrt{\text{Hz}}$ and the input current noise density i_n is 6.9 fA/$\sqrt{\text{Hz}}$

$$
e_n = \Bigg[4kTR_D \left(\frac{R_F}{R_1} + 1 \right)^2 + 4kTR_1 \left(\frac{R_F}{R_1} \right)^2 + 4kTR_F
$$
$$
+ e_n^2 \left(\frac{R_F}{R_1} + 1 \right)^2 + i_n^{+2} R_D^2 \left(\frac{R_F}{R_1} + 1 \right)^2 + i_n^{-2} R_F^2
$$
$$
+ \frac{2qV_bR_D}{R_b + R_D} \Bigg]^{\frac{1}{2}} \frac{\pi}{2} \sqrt{B}. \tag{7}
$$

The feedback resistor R_F and R_1 were chosen to minimize noise in the amplifier circuit. The first term of (7) calculates the Johnson noise contribution of the diode, which is dependent upon the device resistance as well as the feedback circuit. The Johnson noise in R_F and R_1 are calculated by the second and third terms, respectively. The voltage noise of the amplifier is calculated by the fourth term of (7), while the current noise through the + and − terminals of the amplifier are calculated

by the fifth and sixth terms, respectively. The last term of (7) accounts for shot noise when a bias is applied to the device, where V_b is the bias applied through a biasing resistor R_b. Although the above noise analysis is for antenna-coupled MOM diode infrared detectors, it provides consistent results with previous noise analysis for antenna-coupled bolometer infrared detectors [43].

By analyzing the total noise contribution, based on a variable diode resistance, an expected noise contribution can be predicted. For high resistance values, Johnson noise of the diode (arising from R_D) dominates the total noise of the circuit. For diode resistances of 10 kΩ, the amplifier noise begins to rise above the diode Johnson noise. Therefore, for very low resistances (<1 kΩ), the measured device noise would contain a significant noise contribution from the amplifier. The noise of each device was measured with a SR770 FFT Network Analyzer. Fig. 11 shows the Johnson noise and total amplifier noise predictions, along with the measured noise for individual devices. The measured devices were found to follow the Johnson noise prediction, meaning that the amplifier did not impart a significant noise contribution to the devices. Therefore, the first contribution in (7) is dominant.

C. Infrared Characterization

While strong polarization dependence is not in itself indicative of high performance from a device, for antenna-coupled devices it indicates that the device response is due to the antenna. Some work has indicated that laser-induced thermal contributions can be the source of device response, as indicated by a decreasing signal as chopping frequency is increased [9], [44]. However, the response from the diodes fabricated for this paper did not exhibit thermal response behavior. Since the response of the devices is polarization dependent and thermal contributions do not contribute to the signal, this confirms that the response is due to Fermi-level modulation. Fig. 12 shows the polarization-dependent response of a dipole antenna-coupled Al/AlO$_x$/Pt MOM diode.
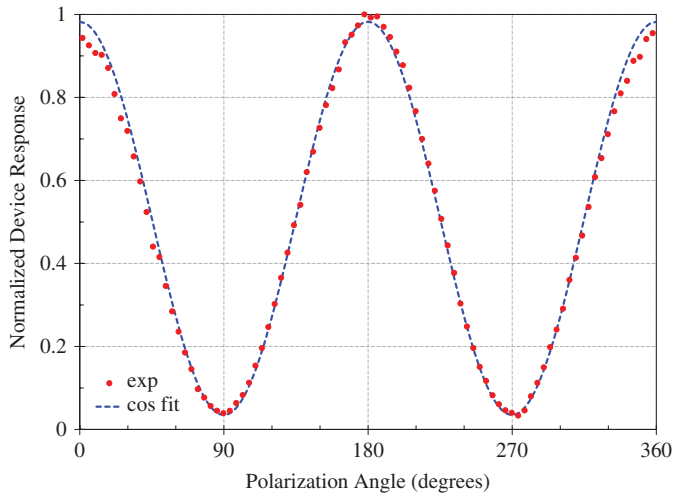
Fig. 12.   Polarization response of an Al/AlO$_x$/Pt ACMOMD. The electric field of the incident radiation is parallel to the antenna at 0°, 180°, and 360°, where the maximum response was measured and at a minimum at 90° and 270° where the incident field is perpendicular to the dipole antenna. The polarization ratio for this device, which is the maximum response divided by the minimum response, is about 8:1.
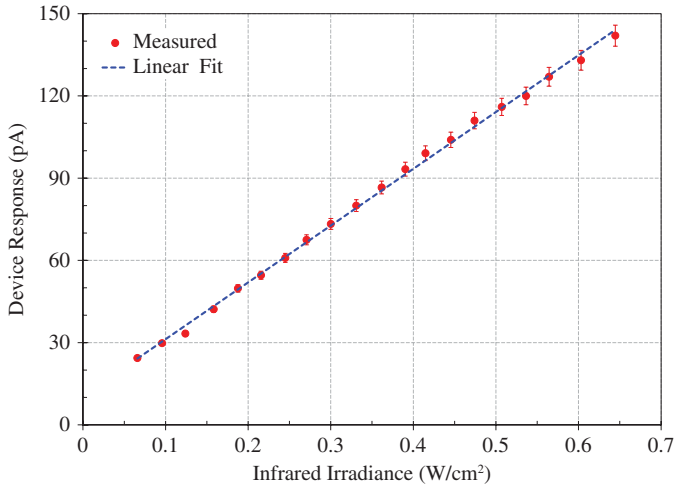

Fig. 13.   Device response as a function of infrared irradiance. The rectified current is proportional to the input power, or the square of the induced voltage shown in (8), which is clearly shown by the measured data.

Fig. 14.   SNR as a function of Al/AlO$_x$/Pt diode nonlinearity. A linear trend with zero intercept is expected from (8), which holds true for nonlinearities less than 10 μA/V^2, corresponding to devices greater than 10 kΩ.

Fig. 15.   Bias-dependent response of an antenna-coupled Al/AlO$_x$/Pt diode. The device response follows the second derivative of the I–V characteristic, as expected from (8).

The response of these devices is based upon the magnitude of the current that is rectified by the MOM diode. This rectified current Ir from the diode is related to the amplitude of the induced infrared voltage from [22, eq. (1)] and is expressed as

$$I_r = \left. \frac{1}{4} \frac{d^2 I}{dV^2} \right|_{V=V_b} V_{IR}^2 \qquad (8)$$

where the second derivative is evaluated at the bias voltage of interest. Since the rectified current is proportional to the square of the induced voltage and thus the incident power, the device operates as a square-law detector. Fig. 13 shows the device response as a function of infrared input power.

Akin to Fig. 13, where the rectified current increases as a function of the incident power, the rectified current is also dependent upon the nonlinearity, or second derivative, of the I–V characteristic. By measuring the devices and comparing the SNR as a function of diode nonlinearity, which is shown
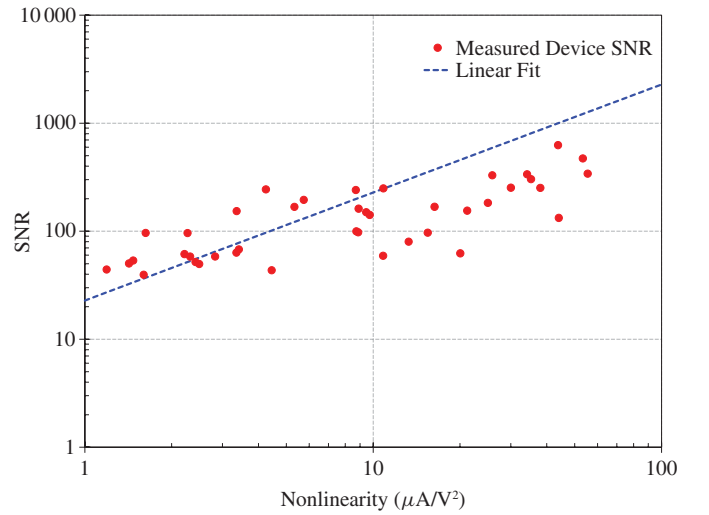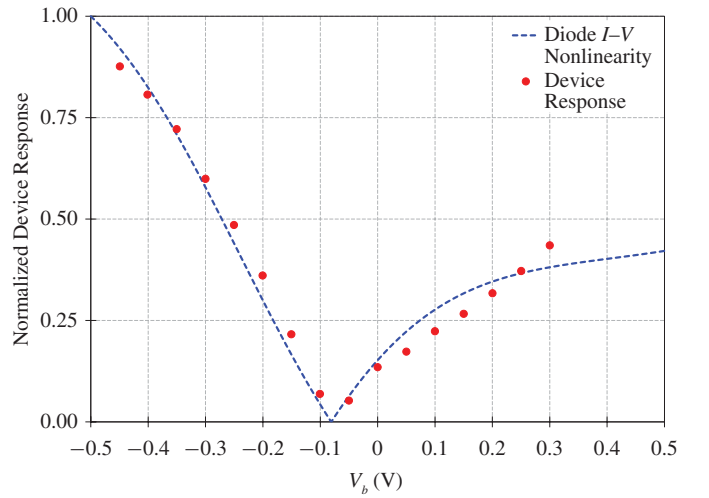
as a function of resistance in Fig. 8. Fig. 14 shows the device SNR as a function of device nonlinearity. While there is some scatter in the data, for device nonlinearities of less than 10 μA/V^2, which corresponds to device resistances of approximately 20 kΩ and above, the rectified current follows (8). The dashed line in the plot shows a linear fit with a zero intercept. For higher nonlinearity, SNR does not increase linearly. This could be due to several factors, including the fact that these low-resistance devices may have pinholes in the thin oxide barriers [44].

Up to this point, all of the measurements have been performed at zero bias. This has been possible due to the fact that asymmetric diodes have been fabricated and zero-bias nonlinearity is a nonzero quantity. However, it is possible to bias the devices to increase response, by moving along the nonlinearity curve, similar to that shown in Fig. 7(c). Fig. 15 shows the dependence of device response as a function of bias voltage V_b. V_b was swept in 50-mV steps and the response was
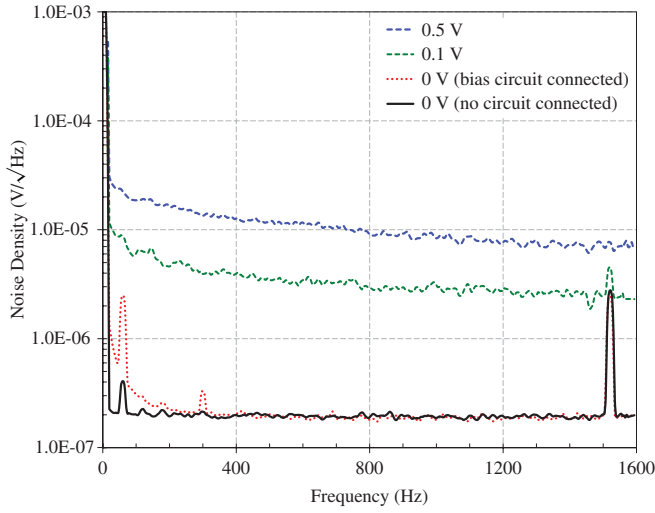
Fig. 16. Output voltage density as a function of a frequency measured with a network analyzer. The signal due to incident radiation is shown at the chopping frequency, which is approximately 1525 Hz.
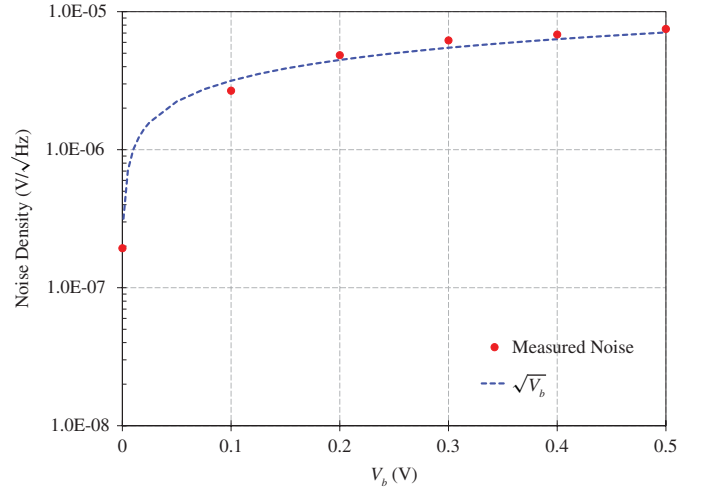

Fig. 17. Voltage noise density at 1582 Hz as a function of a bias measured with a network analyzer. The noise density at zero bias is equal to the Johnson noise of the diode. As the device is biased, shot noise increases the noise of the device.

recorded. The response of the device, shown by the data points, is proportional to the device nonlinearity, which is shown as the line. The maximum bias in the forward direction could only be increased to 0.3-V due to the nonlinear resistance of the device. However, the expected trend is still evident.

It was found that, for unbiased measurements, Johnson noise of the diode was the dominant noise source, shown in Fig. 11. When the device is biased, shot noise is introduced, which is represented by the last term in (7). $1/f$ noise is also introduced, but a low-pass filter was used to minimize fluctuations of the bias source. The output voltage density of the current preamplifier as a function of frequency can be seen in Fig. 16, which was captured by a network analyzer. This device has a zero-bias resistance of 25.5 kΩ.

The measured data at zero bias is shown here for two cases, both with (dotted red line) and without the bias (solid black line) circuit connected. With the bias circuit connected, a slight increase in $1/f$ noise is seen, as well as an increase at 60 Hz due to line noise in the cabling and electrical connections. $1/f$ noise and shot noise that arises due to current flow through the device increase as a small bias (0.1-V) is applied on the device. The signal due to the incident infrared radiation also increases, following the expected trend due to the increase in device non-linearity. As the device bias is further increased, the shot noise increases to a level higher than that due to incident radiation.

Fig. 17 shows the measured noise density at 1582 Hz as a function of bias for the same device measured in Fig. 16. At zero bias, the measured noise is due to Johnson noise of the diode. As the device is biased, the voltage noise density increases proportionally to the square root of the applied bias as shown by the last term (shot noise) in (7).

For Al/AlO$_x$/Pt diodes, the large work function difference leads to a high built-in field. This allows these asymmetric devices to detect LWIR radiation without bias, which has been determined to be the optimum operating point. However, devices fabricated using a different material set would result in a different *I–V* characteristic and device nonlinearity, and

hence might allow for the use of biasing to increase SNR compared to that achievable with unbiased operation.

Using the measured SNR, detector area, and infrared flux on the detector, the noise equivalent power (NEP) and specific detectivity (D*) can be calculated [45]. The effective area for these antenna-based devices, which is the area for which response is due to the antenna as measured, is elliptical in shape and approximately 61 μm^2 [46]. For an unbiased Al/AlO$_x$/Pt device on the substrate detailed in the fabrication section with 4.23 W/cm^2 infrared irradiance in an approximately diffraction limited F/8 beam, the measured SNR is 626, NEP is 4.11 nW, and D* is 1.91×10^5 cm·Hz$^{1/2}$·W^{-1}.

D* can be improved in a number of ways. The D* and associated measurements quoted above are for air-side illumination. The use of a Ge hemispherical immersion lens, with illumination through the substrate, has been previously demonstrated [47] to increase the signal level by a factor of 50. Given this, Al/AlO$_x$/Pt devices were measured in this configuration and a D* of 9.65×10^6 cm·Hz$^{\frac{1}{2}}$·W^{-1} was obtained, which is the highest D* reported to date for antenna-coupled IR MOM diode infrared detectors. Further, there exists an impedance mismatch between the antenna and the diode. By fabricating antennas that have a higher feed point impedance, and matching the diode impedance using the controlled oxidation process set out in this paper, a higher portion of the resonant antenna currents could be rectified by the diode, which stands to further improve the D*.

V. CONCLUSION

The study detailed in this paper has shown the ability to tailor response characteristics of Al/AlO$_x$/Pt antenna-coupled MOM diodes based on the oxidation which forms the tunnel barrier in the MOM diode. It has been shown that the *I–V* characteristics can be tailored so that a desired resistance or nonlinearity can be achieved by controlling the oxidation pressure. By characterizing the noise, it was determined that for unbiased device measurements, the dominant device noise

is due to Johnson noise of the diode. This noise can be reduced by reducing the resistance of the diode, and as such the SNR increases for low resistance, or high nonlinearity, devices. However, devices with resistance less than 10 kΩ, where the tunneling barrier is very thin, can exhibit abnormal device performance due to "hot spots." Biasing these devices showed that detected signal increases as a function of the diode nonlinearity, but that SNR suffers due to the introduction of shot noise. Using different materials or fabrication techniques for the device would lead to a different I–V characteristic and therefore device nonlinearity. If the nonlinearity of the device were to increase with bias faster than the associated $1/f$ and shot noise, SNR would increase as a function of bias. Device response as a function of irradiance, nonlinearity, and bias were shown for Al/AlO$_x$/Pt devices, device response was maximized according to application and noise constraints, and D* was improved for this detector technology.

VI. Acknowledgment

References

[1] C. Fumeaux, W. Herrmann, H. Rothuizen, P. De Natale, and F. K. Kneubühl, "Mixing of 30 THz laser radiation with nanometer thin-film Ni-NiO-Ni diodes and integrated bow-tie antennas," *Appl. Phys. B: Lasers Opt.*, vol. 63, no. 2, pp. 135–140, Aug. 1996.

[2] I. Codreanu, F. González, and G. Boreman, "Detection mechanisms in microstrip dipole antenna-coupled infrared detectors," *Infrared Phys. & Technol.*, vol. 44, no. 3, pp. 155–163, Jun. 2003.

[3] P. C. Hobbs, R. B. Laibowitz, and F. R. Libsch, "Ni-NiO-Ni tunnel junctions for terahertz and infrared detection," *Appl. Opt.*, vol. 44, no. 32, pp. 6813–6822, Nov. 2005.

[4] P. Esfandiari, G. Bernstein, P. Fay, W. Porod, B. Rakos, A. Zarandy, B. Berland, L. Boloni, G. Boreman, B. Lail, B. Monacelli, and A. Weeks, "Tunable antenna-coupled metal-oxide-metal (MOM) uncooled IR detector," in *Proc. SPIE, Infrared Technol. Appl. XXXV*, vol. 5783. Bellingham, WA, Jun. 2005, pp. 470–482.

[5] J. A. Bean, B. Tiwari, G. H. Bernstein, P. Fay, and W. Porod, "Thermal infrared detection using dipole antenna-coupled metal-oxide-metal diodes," *J. Vac. Sci. Technol. B: Microelectron. Nanometer Struct.*, vol. 27, no. 1, pp. 11–14, Jan. 2009.

[6] B. Tiwari, J. A. Bean, G. Szakmany, G. H. Bernstein, P. Fay, and W. Porod, "Controlled etching and regrowth of tunnel oxide for antenna-coupled metal-oxide-metal diodes," *J. Vac. Sci. Technol. B: Microelectron. Nanometer Struct.*, vol. 27, no. 5, pp. 2153–2160, Sep. 2009.

[7] S. Y. Wang, T. Izawa, and T. K. Gustafson, "Coupling characteristics of thin-film metal-oxide-metal diodes at 10.6 μm," *Appl. Phys. Lett.*, vol. 27, no. 9, pp. 481–483, Nov. 1975.

[8] M. Heiblum, S. Y. Wang, T. K. Gustafson, and J. R. Whinnery, "IIb-7 edge-MOM diode: An integrated, optical, nonlinear device," *IEEE Trans. Electron Devices*, vol. 24, no. 9, pp. 1199–1199, Sep. 1977.

[9] M. Heiblum, W. Shihyuan, J. R. Whinnery, and T. K. Gustafson, "Characteristics of integrated MOM junctions at DC and at optical frequencies," *IEEE J. Quantum Electron.*, vol. 14, no. 3, pp. 159–169, Mar. 1978.

[10] C. Fumeaux, W. Herrmann, F. K. Kneubühl, and H. Rothuizen, "Nanometer thin-film Ni-NiO-Ni diodes for detection and mixing of 30 THz radiation," *Infrared Phys. & Technol.*, vol. 39, no. 3, pp. 123–183, Apr. 1998.

[11] C. Fumeaux, G. Boreman, W. Herrmann, H. Rothuizen, and F. Kneubühl, "Polarization response of asymmetric-spiral infrared antennas," *Appl. Opt.*, vol. 36, no. 25, pp. 6485–6490, Sep. 1997.

[12] C. Fumeaux, J. Alda, and G. D. Boreman, "Lithographic antennas at visible frequencies," *Opt. Lett.*, vol. 24, no. 22, pp. 1629–1631, Nov. 1999.

[13] M. R. Abdel-Rahman, F. González, and G. D. Boreman, "Antenna-coupled metal-oxide-metal diodes for dual-band detection at 92.5 GHz and 28 THz," *Electron. Lett.*, vol. 40, no. 2, pp. 116–118, Jan. 2004.

[14] I. Wilke, W. Herrmann, and F. K. Kneubühl, "Integrated nanostrip dipole antennas for coherent 30 THz infrared radiation," *Appl. Phys. B: Lasers Opt.*, vol. 58, no. 2, pp. 87–95, Feb. 1994.

[15] I. Wilke, Y. Oppliger, W. Herrmann, and F. K. Kneubühl, "Nanometer thin-film Ni-NiO-Ni diodes for 30 THz radiation," *Appl. Phys. A: Mater. Sci. Process.*, vol. 58, no. 4, pp. 329–341, Apr. 1994.

[16] M. Abdel-Rahman, B. Monacelli, A. Weeks, G. Zummo, and G. Boreman, "Design, fabrication and characterization of antenna-coupled metal-oxide-metal diodes for dual-band detection," *Opt. Eng.*, vol. 44, no. 6, pp. 066401-1–066401-7, Jun. 2005.

[17] J. W. Dees, "Detection and harmonic generation in the sub-millimeter wavelength region," *J. Microw.*, vol. 9, pp. 48–55, Sep. 1966.

[18] L. O. Hocker, D. R. Sokoloff, V. Daneu, A. Szoke, and A. Javan, "Frequency mixing in the infrared and far-infrared using a metal-to-metal point contact diode," *Appl. Phys. Lett.*, vol. 12, no. 12, pp. 401–402, Jun. 1968.

[19] K. M. Evenson, J. S. Wells, and L. M. Matarrese, "Absolute frequency measurements of the CO$_2$ CW laser at 28 THz (10.6 μm)," *App. Phys. Lett.*, vol. 16, no. 6, pp. 251–253, Mar. 1970.

[20] S. I. Green, "Point contact MOM tunneling detector analysis," *J. Appl. Phys.*, vol. 42, no. 3, pp. 1166–1169, Mar. 1971.

[21] B. Rakos, H. Yang, J. Bean, G. H. Bernstein, P. Fay, and W. Porod, "Investigation of antenna-coupled MOM diodes for infrared sensor applications," in *Proc. 14th Int. Conf. Nonequilibrium Carrier Dynamics Semicond.*, vol. 110. Dec. 2005, pp. 105–108.

[22] S. Faris, T. Gustafson, and J. Wiesner, "Detection of optical and infrared radiation with DC-biased electron-tunneling metal-barrier-metal diodes," *IEEE J. Quantum Electron.*, vol. 9, no. 7, pp. 737–745, Jul. 1973.

[23] E. Sakuma and K. M. Evenson, "Characteristics of tungsten-nickel point contact diodes used as laser harmonic-generator mixers," *IEEE J. Quantum Electron.*, vol. 10, no. 8, pp. 599–603, Aug. 1974.

[24] A. Sanchez, C. F. Davis, Jr., K. C. Liu, and A. Javan, "The MOM tunneling diode: Theoretical estimate of its performance at microwave and infrared frequencies," *J. Appl. Phys.*, vol. 49, no. 10, pp. 5270–5277, Oct. 1978.

[25] J. R. Tucker and M. F. Millea, "Photon detection in nonlinear tunneling devices," *Appl. Phys. Lett.*, vol. 33, no. 7, pp. 611–613, Oct. 1978.

[26] A. Thon, M. Merschdorf, W. Pfeiffer, T. Klamroth, P. Saalfrank, and D. Diesing, "Photon-assisted tunneling versus tunneling of excited electrons in metal-insulator-metal junctions," *Appl. Phys. A: Mater. Sci. Process.*, vol. 78, no. 2, pp. 189–199, Jan. 2004.

[27] D. Diesing, M. Merschdorf, A. Thon, and W. Pfeiffer, "Identification of multiphoton induced photocurrents in metal-insulator-metal junctions," *Appl. Phys. B: Lasers Opt.*, vol. 78, nos. 3–4, pp. 443–446, Feb. 2004.

[28] H. M. Gupta and R. J. Van Overstraeten, "Role of trap states in the insulator region for MIM characteristics," *J. Appl. Phys.*, vol. 46, no. 6, pp. 2675–2682, Jun. 1975.

[29] K. Gloos, P. J. Koppinen, and J. P. Pekola, "Properties of native ultrathin aluminium oxide tunnel barriers," *J. Phys.: Condens. Matter*, vol. 15, no. 10, pp. 1733–1746, Mar. 2003.

[30] S. Yngvesson, *Microwave Semiconductor Devices*. Norwell: Kluwer, 1991, ch. 4.

[31] J. G. Simmons, "Electric tunnel effect between dissimilar electrodes separated by a thin insulating film," *J. Appl. Phys.*, vol. 34, no. 9, pp. 2581–2590, Sep. 1963.

[32] V. Daneu, D. Sokoloff, A. Sanchez, and A. Javan, "Extension of laser harmonic-frequency mixing techniques into the 9 μm region with an infrared metal-metal point-contact diode," *Appl. Phys. Lett.*, vol. 15, no. 12, pp. 398–401, Dec. 1969.

[33] T. K. Gustafson and T. J. Bridges, "Radiation of difference frequencies produced by mixing in metal-barrier-metal diodes," *Appl. Phys. Lett.*, vol. 25, no. 1, pp. 56–59, Jul. 1974.

[34] B. Twu and S. E. Schwarz, "Mechanism and properties of point-contact metal-insulator-metal diode detectors at 10.6 μm," *Appl. Phys. Lett.*, vol. 25, no. 10, pp. 595–598, Nov. 1974.

[35] D. R. Sokoloff, A. Sanchez, R. M. Osgod, and A. Javan, "Extension of laser harmonic-frequency mixing into the 5-μ regions," *Appl. Phys. Lett.*, vol. 17, no. 6, pp. 257–259, Sep. 1970.

[36] T. K. Gustafson, R. V. Schmidt, and J. R. Perucca, "Optical detection in thin-film metal-oxide-metal diodes," *Appl. Phys. Lett.*, vol. 24, no. 12, pp. 620–622, Jun. 1974.

[37] H. Momida, T. Hamada, and T. Ohno, "First-principles study of dielectric properties of amorphous high-k materials," *Jpn. J. Appl. Phys.*, vol. 46, no. 5, pp. 3255–3260, May 2007.

[38] G. J. Dolan, "Offset works for lift-off photoprocessing," *Appl. Phys. Lett.*, vol. 31, no. 5, pp. 337–339, Sep. 1977.

[39] M. Ohring, *The Materials Science of Thin Films*. New York: Academic, 1992, pp. 53–55.

[40] E. K. Lindmark, J. J. Nowak, and M. T. Kief, "In-situ ellipso-metric measurements of thin film aluminum oxidation," in *Proc. SPIE, Opt. Metrol. Roadmap Semicond., Opt., Data Storage Ind.*, vol. 4099. Nov. 2000, pp. 218–227.

[41] B. M. Kale, "Electron tunneling devices in optics," *Opt. Eng.*, vol. 24, no. 2, pp. 267–274, 1985.

[42] V. Da Costa, F. Bardou, C. Beal, Y. Henry, J. P. Bucher, and K. Ounadjela, "Nanometric cartography of tunnel current in metal-oxide junctions," *J. Appl. Phys.*, vol. 83, no. 11, pp. 6703–6705, Jun. 1998.

[43] F. J. González, "Noise measurements in optical detectors," *Revista Mexicana de Fisica*, vol. 52, no. 6, pp. 550–554, Dec. 2006.

[44] J. G. Small, G. M. Elchinger, A. Javan, A. Sanchez, F. J. Bachner, and D. L. Smythe, "AC electron tunneling at infrared frequencies: Thin-film M-O-M diode structure with broad-band characteristics," *Appl. Phys. Lett.*, vol. 24, no. 6, pp. 275–279, Mar. 1974.

[45] E. L. Dereniak and G. D. Boreman, *Infrared Detectors and Systems*. New York: Wiley, 1996, pp. 202–205.

[46] C. Fumeaux, G. Boreman, W. Herrmann, F. Kneubühl, and H. Rothuizen, "Spatial impulse response of lithographic infrared antennas," *Appl. Opt.*, vol. 38, no. 1, pp. 37–46, Jan. 1999.

[47] B. Slovick, P. Krenz, G. Zummo, and G. Boreman, "Evaporation of uniform antireflection coatings on hemispherical lenses to enhance infrared antenna gain," *Infrared Phys. & Technol.*, vol. 53, no. 2, pp. 89–93, Mar. 2010.

Arthur Weeks (M'88–SM'05) received the Ph.D. degree in electrical engineering from the University of Central Florida, Orlando, in 1987.

He left the position of Vice President of Corporate Technology at Invivo Research Inc., Orlando, to join the Department of Electrical Engineering, University of Central Florida, as an Associate Professor. He spent one year at the Royal Signals and Radar Establishment in Malvern, Worcestershire, England, studying laser beam propagation. His current research interests include color image processing techniques, reduction of noise within images using adaptive nonlinear filters, and the use of artificial neural networks in pattern recognition.

Dr. Weeks is a member of the Society of Photo-Optical Instrumentation Engineers and Tau Beta Pi.

Jeffrey A. Bean (S'01–M'09) was born in Casper, in 1981. He received the B.S. degree in electrical engineering from the University of Wyoming, Laramie, in 2003, and the M.S. and Ph.D. degrees from the University of Notre Dame, Notre Dame, IN, in 2005 and 2009, respectively.

He is currently a Post-Doctoral Research Associate at the Center for Research and Education in Optics and Laser, University of Central Florida, Orlando, where he is conducting research on antenna-coupled metal-oxide-metal diodes for IR detection. His current research interests include the simulation, fabrication, and characterization of high-speed antenna-based IR detectors.

Glenn Boreman (S'80–M'84–SM'05) received the B.S. degree in optics from the University of Rochester, Rochester, NY, and the Ph.D. degree in optics from the University of Arizona, Tucson.

He is currently a Trustee Chair Professor of optics at the University of Central Florida, Orlando, Center for Research and Education in Optics and Laser. He has been a Visiting Scholar at Imperial College, London, U.K., the Swiss Federal Institute of Technology, Zürich, Switzerland, Complutense University, Madrid, Spain, the University of New Mexico, Albuquerque, and the Totalförsvarets forskningsinstitut (the Swedish Defense Research Agency), Linköping, Sweden. He is a co-author of *Infrared Detectors and Systems* and the author of *Modulation Transfer Function in Optical and Electro-Optical Systems* and *Basic Electro-Optics for Electrical Engineers*.

Prof. Boreman is a Fellow of the Military Sensing Symposium, the Optical Society of America, and the Society of Photo-Optical Instrumentation Engineers. He served for six years as the Editor-in-Chief of *Applied Optics* and is currently an Associate Editor of *Optics Express* and the Editor of the Wiley Series in *Pure & Applied Optics*.